POROSITY AND SURFACE CURVATURE EFFECTS ON THE PERMEABILITY AND WALL SHEAR STRESS OF TRABECULAR BONE: GUIDELINES FOR BIOMIMETIC SCAFFOLDS FOR BONE REPAIR

Zhuang Xiong, Léa Rouquier, Xingrong Huang, Esther Potier, Morad Bensidhoum, Thierry Hoc

POROSITY AND SURFACE CURVATURE EFFECTS ON THE PERMEABILITY AND WALL SHEAR STRESS OF TRABECULAR BONE: GUIDELINES FOR BIOMIMETIC SCAFFOLDS FOR BONE REPAIR

Authors : Zhuang Xiong[1], Léa Rouquier[1], Xingrong Huang[2], Esther Potier[1], Morad Bensidhoum[1], Thierry Hoc [1, 3,*]

Affiliations:

1: Laboratory of Bioengineering and Bioimaging for Osteo-Articular tissues UMR 7052 CNRS, Univ Paris Diderot, Sorbonne Paris Cité, France

2: Laboratory Ecole Centrale de Pékin/School of General Engineering, Beihang University, 100191 Beijing, China

3: Mechanical Department, MSGMGC, Ecole Centrale de Lyon, 69134 Ecully, France …

Key words: bone allografts; surface curvature; computational fluid dynamics; wall shear stress

Abstract: Scaffolds are an essential component of bone tissue engineering to provide support and create a physiological environment for cells. Biomimetic scaffolds are a promising approach to fulfill the requirements. Bone allografts are widely used scaffolds due to their mechanical and structural characteristics. The scaffold geometry is well known to be an important determinant of induced mechanical stimulation felt by the cells. However, the impact of allograft geometry on permeability and wall shear stress distribution is not well understood. This information is essential for designing biomimetic scaffolds that provide a suitable environment for cells to proliferate and differentiate. The present study investigates the effect of geometry on the permeability and wall shear stress of bone allografts at both macroscopic and microscopic scales. Our results concluded that the wall shear stress was strongly correlated with the porosity of the allograft. The level of wall shear stress at a local scale was also determined by the surface curvature characteristics. The results of this study can serve as a guideline for future biomimetic scaffold designs that provide a mechanical environment favorable for osteogenesis and bone repair.

Introduction:

Bone tissue serves multiple functions in the human body, including structural support and muscle attachment. It is a highly dynamic tissue that undergoes remodeling throughout life and has the capacity for self-healing [1]. However, this capacity becomes limited when bone lesions are extensive. The primary focus of bone tissue engineering is to develop therapeutic alternatives to improve repair of large bone defects. One promising strategy for engineering bone is to associate mimetic bone scaffolds, bone progenitor cells and soluble factors to create an environment suitable for osteogenesis [2].

Scaffolds are an essential component of bone tissue engineering as they provide support for cell proliferation and differentiation, as well as promote vessel and nerve growth. It is important that they have the appropriate porosity, bone surface area to volume ratio, mechanical behavior, and biocompatibility for the intended clinical use [3]. Autografts, allografts, and synthetic substitutes are the three major types of scaffolds used for bone defect repair. Autologous bone grafts are considered the gold standard due to their satisfying osteoconduction and osteoinduction properties. However, their application is limited due to their restricted availability and donor site morbidity. Although synthetic substitutes are a promising alternative to autografts, they are typically only osteoconductive and so far displayed inadequate biomechanical properties. As a compromise between these two approaches (autograft versus synthetic substitute), allografts are good candidates. Allografts are cancellous bone fragments harvested from living or deceased donors that have a similar biochemical composition and can create biomechanical conditions that resemble the in vivo environment. As a result, they are widely used in clinical practice for fracture repair [3–5]. Because allografts are believed to recreate a suitable environment for bone cells, conducting researches on the mechanical environment induced by fluid flow in these allografts will help design and fabricate biomimetic scaffolds, especially for in vitro studies such as the development of a bone organoid in a perfusion bio-reactor [6–8].

The design and properties of scaffolds play a crucial role in tissue engineering and regenerative medicine. As previously stated, a scaffold must possess suitable properties to establish an appropriate biological, biochemical, and biomechanical environment for the cells. While the biological and biochemical properties are primarily related to the material's chemical composition, the biomechanical property is believed to be associated with the geometry of the scaffolds. As bone cells are mechanosensitive cells responsive to both strain and shear stresses [9–12], scaffolds with different geometries, resulting in different mechanical environments, will induce different cellular behaviors.

The mechanical environment created by scaffolds can be described at both macroscopic and microscopic scales. At the macroscopic level, it is important to consider the mechanical strength and permeability of the scaffolds. The scaffolds must be resistant enough to bear the loads at the implant site, while also allowing for efficient nutrient transport to the cells. Extensive studies have been performed to evaluate the permeability of natural bones, both experimentally and numerically. The reported magnitude for the permeability of human bone is of 1-743 10-10 m2, depending on the sampling sites [13–18]. The permeability of natural bones has also been found to be anisotropic and dependent on its fabric tensor, trabecular spacing, and structure model index (SMI) [19,20]. At the microscopic level, it is important to determine the strain and stress distribution to assess whether the local mechanobiological environment is suitable for the cells. Several in vitro studies have shown that the range of wall shear stress promoting osteogenesis is of 0.1 – 10 mPa [21–23]. However, this result also depends on the experimental settings, scaffold composition, and scaffold geometry [24–26].

Numerous studies have been conducted to examine the impact of various geometry of synthetic substitutes on bone cell behavior [27–31]. Fan et al. [30], for example, showed that greater scaffold permeability enhanced the growth of osteoblastic cells. Rubert et al. [31] tested different scaffold pore geometries and observed distinct cell activity and bone-like tissue formation outcomes. The results of these studies illustrate the importance of optimal geometry design for synthetic substitutes. However, these different geometries are still simplified versions of the complex structure of bones. Furthermore, human bones have a wider variety of microstructures compared to synthetic substitutes that could potentially affect cellular behaviors. In addition, many studies focus solely on macroscopic properties [18,32,33], with only a limited number of studies examining at microscopic scale [34–36]. In fact, the characterization of the mechanical properties at the microscopic scale is also essential to help understand the stimulation experienced by the cells.

The present study investigates the effect of scaffold geometry on the permeability and wall shear stress of bone allografts at both macroscopic and microscopic scales. Microarchitectural bone allografts parameters were derived from micro-CT images, while surface curvatures calculated from finite element simulations were used to describe the local geometry of allografts. Computational fluid dynamics (CFD) analysis was performed to calculate the permeability at the macroscopic scale, as well as the wall shear stress of allografts at the microscopic scale. It is believed that the results of this study will help gain insights on how the permeability and wall shear stress felt by the cells are influenced by the geometry of the allografts. The permeability and wall shear stress felt by the cells will be referred to as “mechanical properties” in the present study. The findings will thus provide guidelines for designing optimal biomimetic synthetic substitutes in the future for bone defect repair.

Materials and Methods:

1/ Sample preparation

Twenty-nine bone allografts used in the present study were obtained from a bone bank (BioBank, 77127 Lieu-Saint, France) that collects trabecular bone from femoral heads of human donors. The sampling direction and the donor information were not specified. These samples were devitalized and defatted using the Supercrit® inactivation process and sterilized by gamma radiation at 25 kGy [37,38], the bone marrow inside the samples were also removed during the treatment. Then they are cut into cylindrical shapes with a diameter of 6.9 mm and a height of 10 mm as illustrated in Figure 1A using a trephine in a water bath and then air-dried at room temperature from 30 × 20 × 10 mm trabecular bone blocks.

2/ X-ray computed tomography analysis

X-ray computed tomography (micro-CT) was used to obtain the 3D images of the 29 specimens. The micro-CT images were acquired using the Skyscan 1172 micro-CT (Bruker, Kontich, Belgium). The acquisition parameters were set to 40 kV, 100 µA, and a voxel size of 7.9*7.9*7.9 µm corresponding to protocol used in previous study [36]. Then the images were reconstructed with NRecon software (v 1.7.1.0, Bruker, Kontich, Belgium). To avoid boundary effects, a representative cylindrical volume with a diameter of 6 mm and a height of 8 mm was chosen to reconstruct the 3D numerical model for each sample, as illustrated in Figure 1B. The gray level threshold for bone tissue was calculated using the 3D auto-Otsu algorithm integrated in the CTAn software (v. 1.17.7.2, Bruker, Kontich, Belgium).

3/ Computational fluid dynamics analysis

a/ CFD model meshing

In order to reduce the computation cost without losing the structure integrity of the samples, a cubic region of interest in the core area with a length of 4 mm for each section was selected to generate finite element meshes for the computational fluid dynamics (CFD) model. As illustrated in Figure 1C and 1D, the numeric model of fluid domain includes a homogeneous flow layer to facilitate the calculation apart from the trabecular structure.

The 3D images used to reconstruct the fluid domain model meshes were primitively processed with Avizo® software (v. 2021.1, Berlin, Germany). In the first place the “Median filter” module was used to reduce image noises. Then 3D binary images were obtained by using the “Interactive thresholding” module with the threshold calculated by 3D auto-Otsu algorithm, except that it’s the complementary threshold for bone tissue threshold, assuming that the fluid domain occupies the void. Next the “Dilation”, “Erosion”, and “Binary smoothing” modules were employed to smooth the model border and reduce the image pixelization errors. Finally, the “Label analysis” module was used to remove all the non-connected parts of the 3D model.

After the generation of preliminary surface meshes for the 3D models, they were exported in “.stl” format and then imported in FEBioStudio software® (v.2.3) [39]. The 3D models

were then remeshed with tetrahedrons by using the "MMG Remesh" method integrated in the software. According to preliminary simulation results, the remesh parameters were set to have a good compromise between the calculation cost and result reliability, with the element size of 25, min element size of 5, Hausdorff value of 0.2, and gradation of 1.1. The average element numbers for all the models after remesh process are presented in Table 1. For each sample, 4-node tetrahedral with a Gaussian integration point were used for meshing and calculation. Due to the large number of elements, a skin surface with an average thickness of three microns was implemented at the fluid-bone interface. Therefore, due to the small thickness value, it was assumed that the Cauchy stress of an element calculated in this skin surface was equal to the Cauchy stress at the corresponding skin surface.

b/ *Boundary conditions and fluid properties*

CFD simulation of a Newtonian fluid passing through a trabecular bone structure were performed in FEBioStudio software® (v.2.3) as illustrated in Figure 1D. The outlet surface pressure was set at 0 Pa and the no-slip condition was given to the skin surfaces. The inlet velocity normal to the surface was determined at 0.5 mm/s according to the preliminary simulation results of wall shear stress distribution, with the aim to have an osteogenic shear stress ranged from 0.1 mPa to 10 mPa [21–23, 40]. The fluid is adjusted to have mechanical properties similar to those of the αMEM culture medium at ambient temperature: the fluid density was fixed to 1,000 kg/m3, a bulk modulus of 2.2x105 Pa, a bulk viscosity of 0.002 Pa·s, and a shear viscosity of 0.001 Pa·s.

4/ *Calculation of permeability and wall shear stress*

a/ Calculation of the permeability (k)

Considering the fluid domain between the inlet and outlet of the allograft structure, the permeability k of the sample was calculated by using Darcy's law [41]:

$$k = \frac{Q\mu L}{A\Delta p} \quad (1)$$

Where Q is the flow rate of the fluid, μ is the shear viscosity of the fluid, L is the height of the sample, A is the surface area of the flow region, and Δp is the pressure drop of the fluid that was obtained from the simulation results.

b/ Calculation of wall shear stress (WSS)

Bone cells are mechano-sensitive cells that respond to mechanical stimulation such as fluid-induced shear stress. As the cells adhere to the skin surface, the shear stress in the tangential direction to the skinsurface is the most important. Hence, the wall shear stress induced by the fluid should be calculated in the tangential direction rather than the absolute coordinate system directions.

In the absolute three-dimensional coordinate system composed by the three basic vectors $(\vec{x}, \vec{y}, \vec{z})$, the stress vector, $\vec{T} = \vec{x}T_1 + \vec{y}T_2 + \vec{z}T_3$ in Cartesian coordinate, experienced by a finite element can be calculated by equation (2):

$$\vec{T} = \sigma \times \vec{n} = \begin{Bmatrix} \sigma_{xx} & \sigma_{xy} & \sigma_{xz} \\ \sigma_{yx} & \sigma_{yy} & \sigma_{yz} \\ \sigma_{zx} & \sigma_{zy} & \sigma_{zz} \end{Bmatrix} \begin{pmatrix} n_1 \\ n_2 \\ n_3 \end{pmatrix} = \begin{pmatrix} T_1 \\ T_2 \\ T_3 \end{pmatrix} \quad (2)$$

Where σ represents the Cauchy stress tensor of one skin surface finite element, $\vec{n} = \vec{x}n_1 + \vec{y}n_2 + \vec{z}n_3$ is the external normal vector of the skin surface of one skin surface finite element.

Then $\vec{T}$ can be expressed by a combination of its sub-components in the normal direction, the normal stress $\overrightarrow{\sigma_n}$, and in the tangential direction, the wall shear stress (WSS) $\vec{\tau}$ as illustrated in Figure 1F. As shown in equation (3), they can be individually calculated by equations (4) and (5).

$$\vec{T} = \overrightarrow{\sigma_n} + \vec{\tau} \quad (3)$$

$$\overrightarrow{\sigma_n} = \left(\vec{T} \bullet \vec{n}\right) \bullet \vec{n} = \begin{pmatrix} n_1(T_1n_1 + T_2n_2 + T_3n_3) \\ n_2(T_1n_1 + T_2n_2 + T_3n_3) \\ n_3(T_1n_1 + T_2n_2 + T_3n_3) \end{pmatrix} \quad (4)$$

$$\vec{\tau} = \vec{T} - \overrightarrow{\sigma_n} = \begin{pmatrix} T_1 - n_1(T_1n_1 + T_2n_2 + T_3n_3) \\ T_2 - n_2(T_1n_1 + T_2n_2 + T_3n_3) \\ T_3 - n_3(T_1n_1 + T_2n_2 + T_3n_3) \end{pmatrix} = \begin{pmatrix} \tau_1 \\ \tau_2 \\ \tau_3 \end{pmatrix} \quad (5)$$

For a 3D finite element fluid domain model, by knowing the stress tensor and the surface normal for each element in the wall, the WSS for each element was calculated as in equation (6). Since the average height of the skin surface element is of 3 10^{-3} mm, it is assumed that the WSS of this element is equal to the WSS at the skin surface.

$$WSS = |\vec{\tau}| = \sqrt{{\tau_1}^2 + {\tau_2}^2 + {\tau_3}^2} \quad (6)$$

To take into account the effect of element geometry close to the wall, the calculation of the average WSS for a sample needs to be normalized by the individual element, as illustrated in equation (7).

$$\overline{WSS} = \left(\sum |\vec{\tau}| \cdot V_{elem}\right) / \sum V_{elem} \quad (7)$$

Where V_{elem} is the element volume for a finite element at the wall, $\overline{(WSS)}$ denotes the average WSS level for a sample. In the present study, WSS was normalized by the volume of the element and by the area adjacent to the bone. The results obtained using the two different normalization methods show a strong linear correlation. This can be seen in Supplemental Data, Figure S1. Consequently, the normalization of the WSS values by the volume of the element, which was already published in a previous study [11], was applied in the present study.

5/ Calculation of geometrical parameters

a/ Calculation of bone microarchitectural parameters

Three dimensional microarchitectural parameters of each of the twenty-nine samples were calculated in the CTAn software (v. 1.17.7.2) by using the binarized 3D images that were used to construct the 3D model. In the present study, the following parameters were calculated and used [42]: bone volume fraction (BV/TV; %), bone surface-to-volume ratio (BS/BV; mm−1), trabecular separation (Tb.Sp; mm), and degree of anisotropy (DA). The modified formula of DA was used in the present study with a range from 0 to 1, where 0 represents an isotropic structure.

b/ Calculation of local surface curvatures

In addition to the traditional microarchitectural parameters, the local surface curvatures including the first local principal curvature (k1) and second local principal curvature (k2) for each finite element of the 3D fluid domain were exported from FEBioStudio software® (v.2.3) to describe the surface geometry at microscopic level. For each element in the skin surface, its first local principal curvature and second local principal curvature were exported to correlate with the WSS calculation result. In the present study, three different surface curvature features occupying the majority of the skin surface area of the samples, greater than 95%, were distinguished: concave, hyperboloid, and convex. The surface features and their corresponding surface descriptions are illustrated in Table 2. It needs to be noticed that the principal curvatures exported from FEBioStudio software® (v.2.3) describe the fluid domain, hence the characteristics of the surface for the solid domain or the fluid domain are specified in the text.

6/ Statistical analysis

For the Pearson's correlation study, the representative sample size was defined assuming an expected correlation of 0.5, a two-tailed significance level (α) of 0.05, and a power level (1-β) of 80%. This calculation gave a sample size of twenty-nine. Statistical analyses were performed using GraphPad Prism (version 9.2, GraphPad Software, San Diego, CA, USA, www.graphpad.com (accessed on 10 November 2023)). Kruskal-Wallis ANOVA test was performed before comparing the results of two groups by Mann-Whitney tests. In all cases, p values < 0.05 were considered significant.

Results:

1/ Bone allograft microarchitectural and mechanical property parameters

The microarchitectural parameters obtained from 3D images are presented in Figure 2A, 2B, 2C, and 2D. The measured mean values and standard deviations for the 29 samples were equal to 28.9 ± 6.1 % for BV/TV; 0.41 ± 0.06 mm-1 for BS/BV; 0.60 ± 0.10 mm for Tb.Sp; 0.56 ± 0.09 for DA; and 0.42 ± 0.32 for SMI. The bone volume fraction BV/TV has the biggest normalized standard deviation equal to 20%, from a minimal value of 16.2% to a maximal value of 40.8%. The normalized standard deviation for other microarchitectural parameters is between 13% to 16%.

The mechanical properties derived from CFD analysis are presented in Figure 2E and 2F. The mean value and standard deviation for permeability were equal to 3.69 ± 2.64 10-9 m2. A wide variation was observed for permeability, from a minimal value of 0.30 10-9 m2 to a maximal value of 10.99 10-9 m2. On the other hand, the mean value and standard deviation for average WSS were equal to 6.43 ± 2.16 mPa, ranging from 3.59 mPa to 11.81 mPa.

Average values of meshing information, BV/TV, permeability, and WSS are presented in Table 1. The average meshed element number was 9,240,469, with an average skin surface element number of 1,380,499. Their individual meshing information, BV/TV, permeability, and WSS are given in Supplemental Data Table S1.

2/ Relationship between microarchitectural parameters, permeability and WSS

Assuming all the parameters follow a normal distribution, Pearson's linear regressions were primitively performed among the parameters. The correlation matrix for the regression coefficient R values is presented in Figure 3A. The correlation results show that BV/TV is linearly correlated with BS/BV, SMI, and Tb.Sp, but not with DA. The correlation between BV/TV and SMI is given in Supplemental Data Figure S2.

As for the macroscopic mechanical bone properties parameters, the BV/TV is the microarchitectural parameter that is most correlated with k and average WSS. It can be seen that BV/TV is negatively correlated with permeability while positively correlated with the average WSS. However, the correlation relation is stronger for average WSS, with Pearson's value R = 0.84, than for permeability, with Pearson's value R = -0.68. Between permeability and average WSS, the correlation is non-linear. The R-squared value equals to 0.64 when a non-linear one-phase decay exponential regression was performed

3/ CFD analysis of fluid domain

As the BV/TV of an allograft strongly influenced its respective level of average WSS, three representative samples with varying BV/TV were chosen to compare the fluid domain differences in terms of shear stress and fluid velocity. The sample n°29 has a BV/TV of 40.55%, the sample n°10 has a BV/TV of 29.67%, and the sample n°26 has a BV/TV of 21.06%. The distribution of von-Mises stress, maximum shear stress, nodal z fluid velocity, as well as the nodal fluid velocity for these three samples are presented in Figure 4.

In terms of shear stress, it can clearly be seen that the area of higher shear stress decreases as the BV/TV decreases. For sample n°29 (BV/TV=40.55%), high level of shear stress appears at the inlet surface. While for the other two samples, the shear stress level becomes more important in the middle part of the structure. Potentially due to the higher level of BV/TV, the fluid domain of sample n°29 was separated into multiple small sections compared to sample n°26 (BV/TV = 21.06%), which may result in fluid passage difficulties and thus higher shear stresses. Furthermore, the location of the mechanically stimulated areas is different for every slices. This may be due to the high heterogeneity of the 3D structure.

From the fluid velocity profiles, it can be seen that a great proportion of fluid domain has a velocity exceeding the inlet velocity of 0.5 mm/s. This proportion becomes higher when the sample has a higher BV/TV. However, the areas with higher velocity are not necessarily associated with higher shear stress areas.

Figure 5 shows the WSS distribution for the three samples. Near 50% of skin surface area of each sample is within the osteogenic WSS range ([0.1, 10] mPa), with sample n°29 (BV/TV = 40.55%) having the lowest surface area portion that experiences such stimulation. Within the osteogenesis range, 0.4-0.8 mPa WSS represents the range to which most elements are exposed.

4/ Local surface curvature and local fluid-induced shear stress correlation

After examining the fluid domain for a whole allograft, the investigation of the microarchitecture influence on fluid-induced shear stress was carried out on the microscopic level. The Figure 6 shows the local distribution of the Gaussian curvature (K), the mean curvature (H), and the von-Mises stress for a randomly chosen local fluid domain, where the Gaussian curvature and the mean curvature can be calculated according to equations (8) and (9):

$$K = k_1 * k_2 \tag{8}$$

$$H = \frac{1}{2}(k_1 + k_2) \tag{9}$$

As shown in Figure 6A, a great part of the surface has negative value for K while the values of H are mainly positive in Figure 6B. This result means that the trabecular bone surface is mainly composed of hyperboloid surface (K<0). By comparing the local principal curvatures given in Figure 6A, 6B, and the distribution of von-Mises stress given in Figure 6C, a distinct distribution of von-Mises stress can be observed for regions where the local principal curvatures are both negative from regions where they are both positive. The convex regions of the fluid domain experienced a lower level of von-Mises shear stress than the concave regions of the fluid domain.

In order to highlighted the influence of the local surface curvature on the local WSS, three regions with different curvature characteristics for the fluid domain were analyzed: one concave region; one hyperboloid region; and one convex region. The average WSS and the area ratio for the three selected surface curvature types (concave, hyperboloid, and convex) for the 29 individual samples are given in Supplemental Data Table S2. The sums of the area ratios are not equal to 1 because of the four side surfaces with principal curvatures equal to zero. The results are compared for all the 29 samples and it is presented in Figure 7. It can be concluded that there exist significant differences for the average WSS among these three regions of the fluid domain: the concave regions have the highest average WSS, the hyperboloid regions have the second highest while the convex regions have the lowest average WSS. In addition, the average WSS for concave and convex regions have the same distribution characteristics where the density is the highest near the lower quartile. However, the highest density for hyperboloid range appears near its median value.

5/ BV/TV and different curvature regions correlation

To take a step further to see if the porosity will influence the area ratio and average WSS distribution of the selected surface curvature regions, correlation studies were performed and illustrated in Figure 8. It can be observed that the BV/TV is positively correlated with the area ratio for the convex region of the fluid domain, while SMI is negatively correlated with the area ratio for the convex region of the fluid domain. The correlation result is given in Supplemental Data Figure S3. As for the average WSS, it correlates with BV/TV for all the three selected surface curvature regions, which is in accordance that to the finding that BV/TV is correlated with the average WSS of samples. The average WSS of the three regions are strongly correlated with each other, in contrast to the area ratio of the three regions.

Apart from the individual area ratio and average WSS, the ratio of the average WSS between the three selected surface curvature regions were determined. The histograms for the ratios of each sample as well as the Pearson's R-squared values between the BV/TV and the individual ratios are illustrated in Supplemental Data Figure S2. There is no evident correlation found. It can be concluded that with increasing BV/TV, the variation of the ratios for regional average WSS is limited even though the average WSS and the BV/TV are increasing.

Discussion:

In the context of large bone defect repair and bone tissue engineering, scaffolds are essential to provide a suitable 3D environment for cells. Numerous studies have focused on the design of substitute scaffold materials that promote osteoconduction and osteoinduction [43–46]. From a mechanobiological perspective, the mechanical properties of these scaffolds, particularly the fluid-induced WSS and permeability, may be crucial factors that guide cellular behavior and could define the choice of a specific 3D biomimetic scaffold. Therefore, studying the permeability and fluid-induced WSS distribution of human bone allografts can provide insight into the relationship between their geometry and mechanical properties at both the macroscopic and microscopic scales. This information can be used as a reference for the design of 3D synthetic substitutes. In the present study, conventional microarchitectural parameters derived from micro-CT imaging were used to describe the macroscopic geometry, while surface curvatures calculated from finite element models were used to describe the microscopic geometry. Based on a constant flow rate CFD simulation, the permeability and the WSS were calculated for all the samples. The results of the present study emphasized the importance of considering both the scaffold porosity at the macroscopic scale and the surface curvature at the microscopic scale. However, the variation in WSS was limited regardless of the microarchitecture. These findings should be considered when designing scaffolds to create in vitro mechanical environments suitable for osteogenesis, as for the production of a bone organoid using perfusion bioreactor, where the fluid flow will greatly influence the cellular activities [6–8].

At the macroscopic scale, two important mechanical properties that are thought to influence cellular behavior and osteogenesis are permeability and average WSS [47]. Therefore,

careful consideration of their interaction is necessary when designing a scaffold. The BV/TV of the allografts was found to be the most important indicator of these two parameters in the present study. When the bone allograft has a higher BV/TV, its permeability decreases while its average WSS increases. This finding is consistent with the literature and common understanding [47,48]: when there are more obstacles in a volume-fixed structure, the fluid will encounter more resistance and interact more with the surface of the structure. Tb.Sp, BS/BV, SMI, and DA were also found to modulate permeability in the present study, although to a lesser extent. Kreipke et al [20] studied the dependence of permeability on the fabric tensor, trabecular spacing, and SMI and reported that Tb.Sp, SMI, and DA were useful in predicting the permeability of human bones by using the Kozeny-Carman relationship. Our findings support theirs, indicating that the microarchitecture parameters influence the permeability of the scaffold as well. Therefore, it is important to consider the effects of geometry when designing biomimetic scaffolds. The correlation shown in Figure 3 indicates a linear relationship between the BV/TV of allografts and the average WSS. The correlation between permeability and average WSS is exponential rather than linear. When the permeability of the allografts exceeds 5x10-9 m2, the variation in average WSS becomes limited. Therefore, the plateau phase in the exponential correlation can be an ideal range to achieve both optimum permeability and optimum average WSS simultaneously.

Three samples with different BV/TV values were selected to further investigate the influence of BV/TV on the WSS distribution. For all three samples, the surface area ratio decreases monotonically as WSS increases (Figure 5). Multiple studies investigated this distribution of WSS in various triply periodic minimal surface and lattice-based structures. The majority of these structures do not exhibit a monotonic decreasing distribution, with a second or a third peak appearing in different WSS ranges [49,50]. The same distribution trend was also observed in the present study for all three samples when considering the osteogenesis WSS range of [0.1, 10] mPa, with the highest peak occurring in the range of [0.4, 0.8] mPa. It was also found that as BV/TV increased, the proportion of skin surface within the osteogenesis WSS range decreased. However, the proportion of each osteogenesis WSS subrange did not differ greatly between different samples. This result suggests that a high BV/TV level will mostly result in a greater proportion of highly-stimulated (> 10 mPa) skin surfaces, which are more likely to induce chondrogenesis [40,51]. Therefore, a lower BV/TV level for the scaffold may be more suitable for osteogenesis.

At the microscopic scale, the influence of local surface curvature on cell behavior has attracted significant attention. Previous studies have shown that surface curvature characteristics can influence the cell migration, cell proliferation and cell differentiation behaviors [52–54]. Therefore, it is worthwhile to examine this geometric influence from a mechanical perspective to determine whether cells are exposed to varying mechanical stimulation when residing in regions of different curvature. The study of Li et al. [55] already showed that surface curvature significantly affects the mechanical properties and permeability of their synthetic substitutes. In the present study, the three regions with distinct curvature characteristics for the fluid domain (i.e., Concave, Hyper, Convex) exhibited significantly different levels of WSS stimulation for all twenty-nine samples. This indicates that local surface curvature influences the mechanical stimulation induced by the fluidic environment. Previous research showing that cells tend to prefer regions with at least one negative principal curvature [56,57] suggests that cells seeded in the allografts will initially colonize the concave or hyperboloid regions before proliferating and covering other areas. The results of the present study indicate that the cells seed on the allografts will therefore initially experience a higher lower WSS stimulation than the average WSS level. These findings support the idea that consideration of the local curvature characteristics of the scaffold is critical for providing an optimal mechanical environment for the cells.

In addition, correlation analyses were conducted between BV/TV and curvature region characteristics to investigate the potential influence of allograft porosity on its microscopic geometry. Area ratio was positively correlated with BV/TV only for the convex surface curvature regions of the fluid domain. No obvious correlation could be observed for the other two surface curvature regions. On the other hand, BV/TV remained the determining factor for the average WSS of the three surface curvature regions: as BV/TV increased, the average WSS for the three regions also increased. However, as shown in Figure S2, a higher BV/TV does not result in a greater variation of the average WSS ratio between the three surface curvature regions.. This indicates that while a higher BV/TV may result in a higher average level of WSS for all regions in allografts, the variation in the average WSS ratio between different surface curvature regions is still limited. It is hence worth noting that bone allografts extracted from human bones have a morphogenesis tendency that prevents the appearance of regions with extreme WSS values.

The present study has several limitations. Firstly, it did not investigate deeply the influence of other microarchitectural parameters such as BS/BV and Tb.Sp on permeability, despite their potentially determining role, as suggested by the present results and the literature [20]. However, as these parameters are strongly correlated with BV/TV, it is difficult to dissociate the influence of porosity from other microarchitecture parameters. In addition, the aim and novelty of the present study focused mainly on the shear stress experienced by cells on the bone surface, which has been little studied in the literature, unlike scaffold permeability, which has been the subject of extensive studies [13-20]. Secondly, the allografts used in the study were all harvested from the human femoral head. Trabecular bone from other sites such as the iliac bone, vertebrae, or tibia, have different microstructures that may affect the results [58,59]. Hence the results of the current study will only be applicable to scaffolds mimicking femoral head bones. In the future, allografts from various harvesting/collection sites should be included to obtain a more general conclusion regarding the effects of geometry on mechanical properties. The third limitation of the study is that it did not take into account the deformation of the trabecular bone induced by fluid flow. In this study, the trabecular structure was considered as a rigid, undeformable material, whereas in reality it exhibits elastic behaviors. However, the stress induced by fluid is relatively negligible compared to the stress induced by compression in the previous study [36]. Therefore, the results should not be significantly affected without considering fluid-structure interaction.

In conclusion, the present study examined the effect of trabecular bone geometry on permeability and fluid-induced WSS at both the macroscopic and microscopic scales. Micro-CT was used to obtain conventional bone microarchitectural parameters, while finite element were used to obtain the local surface

curvatures. Computational fluid dynamics was used to calculate the permeability and WSS for each allograft sample. The results showed that the mechanical shear stress experienced by bone cells was strongly correlated with the porosity of the allograft. Additionally, the level of WSS at the local scale was determined by the surface curvature characteristics. However, the variation in porosity did not significantly affect the distribution of WSS. The trabecular bone structure naturally reduced the occurrence of extreme stimulation areas. The results of this study may serve as a guideline for future biomimetic scaffold designs that provide a mechanical environment conducive to osteogenesis and bone repair.

Conflict of interest:

The authors declare no conflict of interest.

Acknowledgments:

The authors would like to thank the Smart Bone Organoid project (ANR-21-CE19-0013-01), the Chinese Scholarship Council (CSC), and the National Natural Science Foundation of China (52105083) for their support.

Author Contribution:

Conceptualization, T.H. and M.B.; methodology, Z.X.; software, Z.X.; validation,; E.P., T.H., M.B. and X.H.; formal analysis, Z.X.; investigation, Z.X.; resources, L.R.; data curation, Z.X.; writing-original draft preparation, Z.X.; writing-review and editing, L.R., E.P., M.B., X.H., T.H.; visualization, Z.X.; supervision, E.P., T.H and M.B; project administration, T.H.; funding acquisition, T.H. and M.B. All authors have read and agreed to the published version of the manuscript.

Disclosure Statement

The authors declare no competing financial interests

References:

1. Shapiro F. Bone development and its relation to fracture repair. The role of mesenchymal osteoblasts and surface osteoblasts. Eur Cell Mater. 2008 Apr 1;15:53–76.

2. Moreno Madrid AP, Vrech SM, Sanchez MA, Rodriguez AP. Advances in additive manufacturing for bone tissue engineering scaffolds. Mater Sci Eng C. 2019;100:631–44.

3. Wang W, Yeung KWK. Bone grafts and biomaterials substitutes for bone defect repair: A review. Bioact Mater. 2017 Dec 1;2(4):224–47.

4. Bauer TW, Muschler GF. Bone Graft Materials: An Overview of the Basic Science. Clin Orthop Relat Res. 2000 Feb;371:10–27.

5. Li Z, Du T, Ruan C, Niu X. Bioinspired mineralized collagen scaffolds for bone tissue engineering. Bioact Mater. 2021 May 1;6(5):1491–511.

6. Gardel LS, Serra LA, Reis RL, Gomes ME. Use of Perfusion Bioreactors and Large Animal Models for Long Bone Tissue Engineering. Tissue Eng Part B Rev. 2014 Apr;20(2):126–46.

7. Jasuja H, Kar S, Katti DR, Katti KS. Perfusion bioreactor enabled fluid-derived shear stress conditions for novel bone metastatic prostate cancer testbed. Biofabrication. 2021 Apr;13(3):035004.

8. Schröder M, Reseland JE, Haugen HJ. Osteoblasts in a Perfusion Flow Bioreactor—Tissue Engineered Constructs of TiO2 Scaffolds and Cells for Improved Clinical Performance. Cells. 2022 Jan;11(13):1995.

9. Ehrlich PJ, Lanyon LE. Mechanical Strain and Bone Cell Function: A Review. Osteoporos Int. 2002 Sep;13(9):688–700.

10. Isaksson H, Nagao S, Małkiewicz M, Julkunen P, Nowak R, Jurvelin JS. Precision of nanoindentation protocols for measurement of viscoelasticity in cortical and trabecular bone. J Biomech. 2010 Aug 26;43(12):2410–7.

11. Becquart P, Cruel M, Hoc T, Sudre L, Pernelle K, et al. Human mesenchymal stem cell responses to hydrostatic pressure and shear stress. Eur Cell Mater. 2016 Feb 19;31:160–73.

12. Stoltz JF, Magdalou J, George D, Chen Y, Li Y, De Isla N, et al. Influence of mechanical forces on bone: Introduction to mechanobiology and mechanical adaptation concept. J Cell Immunother. 2018 Sep 1;4(1):10–2.

13. Beaudoin AJ, Mihalko WM, Krause WR. Finite element modelling of polymethylmethacrylate flow through cancellous bone. J Biomech. 1991 Jan 1;24(2):127–36.

14. Grimm MJ, Williams JL. Measurements of permeability in human calcaneal trabecular bone. J Biomech. 1997 Jul 1;30(7):743–5.

15. Nauman EA, Fong KE, Keaveny TM. Dependence of Intertrabecular Permeability on Flow Direction and Anatomic Site. Ann Biomed Eng. 1999 Jul 1;27(4):517–24.

16. Ochia RS, Ching RP. Hydraulic Resistance and Permeability in Human Lumbar Vertebral Bodies. J Biomech Eng. 2002 Sep 30;124(5):533–7.

17. Baroud G, Falk R, Crookshank M, Sponagel S, Steffen T. Experimental and theoretical investigation of directional permeability of human vertebral cancellous bone for cement infiltration. J Biomech. 2004 Feb 1;37(2):189–96.

18. Syahrom A, Abdul Kadir MR, Abdullah J, Öchsner A. Permeability studies of artificial and natural cancellous bone structures. Med Eng Phys. 2013 Jun;35(6):792–9.

19. Kohles SS, Roberts JB, Upton ML, Wilson CG, Bonassar LJ, Schlichting AL. Direct perfusion measurements of cancellous bone anisotropic permeability. J Biomech. 2001 Sep 1;34(9):1197–202.

20. Kreipke TC, Niebur GL. Anisotropic Permeability of Trabecular Bone and its Relationship to Fabric and Architecture: A Computational Study. Ann Biomed Eng. 2017 Jun 1;45(6):1543–54.

21. Melke J, Zhao F, van Rietbergen B, Ito K, Hofmann S. Localisation of mineralised tissue in a complex spinner flask environment

correlates with predicted wall shear stress level localisation. Eur Cell Mater. 2018 Jul 31;36:57–68.

22. Liu L, Yuan W, Wang J. Mechanisms for osteogenic differentiation of human mesenchymal stem cells induced by fluid shear stress. Biomech Model Mechanobiol. 2010 Dec 1;9(6):659–70.

23. Wittkowske C, Reilly GC, Lacroix D, Perrault CM. In Vitro Bone Cell Models: Impact of Fluid Shear Stress on Bone Formation. Front Bioeng Biotechnol. 2016 ;4. Available from: https://www.frontiersin.org/articles/10.3389/fbioe.2016.00087

24. Porter B, Zauel R, Stockman H, Guldberg R, Fyhrie D. 3-D computational modeling of media flow through scaffolds in a perfusion bioreactor. J Biomech. 2005 Mar 1;38(3):543–9.

25. Stops AJF, McMahon LA, O'Mahoney D, Prendergast PJ, McHugh PE. A Finite Element Prediction of Strain on Cells in a Highly Porous Collagen-Glycosaminoglycan Scaffold. J Biomech Eng. 2008 Dec 1;130(6):061001.

26. Jungreuthmayer C, Donahue SW, Jaasma MJ, Al-Munajjed AA, Zanghellini J, Kelly DJ, et al. A Comparative Study of Shear Stresses in Collagen-Glycosaminoglycan and Calcium Phosphate Scaffolds in Bone Tissue-Engineering Bioreactors. Tissue Eng Part A. 2009 May;15(5):1141–9.

27. McCoy R j., Jungreuthmayer C, O'Brien F j. Influence of flow rate and scaffold pore size on cell behavior during mechanical stimulation in a flow perfusion bioreactor. Biotechnol Bioeng. 2012;109(6):1583–94.

28. Nguyen TD, Kadri OE, Sikavitsas VI, Voronov RS. Scaffolds with a high surface area-to-volume ratio and cultured under fast flow perfusion result in optimal O2 delivery to the cells in artificial bone tissues. Appl Sci Switz. 2019;9(11).

29. Charbonnier B, Manassero M, Bourguignon M, Decambron A, El-Hafci H, Morin C, et al. Custom-made macroporous bioceramic implants based on triply-periodic minimal surfaces for bone defects in load-bearing sites. Acta Biomater. 2020 Jun 1;109:254–66.

30. Fan J, Jia X, Huang Y, Fu BM, Fan Y. Greater scaffold permeability promotes growth of osteoblastic cells in a perfused bioreactor. J Tissue Eng Regen Med. 2015;9(12):E210–8.

31. Marina R. Scaffold pore geometry guides gene regulation and bone-like tissue formation in dynamic cultures.

32. Teo JCM, Teoh SH. Permeability study of vertebral cancellous bone using micro-computational fluid dynamics. Comput Methods Biomech Biomed Engin. 2012 Apr;15(4):417–23.

33. Sandino C, Kroliczek P, McErlain DD, Boyd SK. Predicting the permeability of trabecular bone by micro-computed tomography and finite element modeling. J Biomech. 2014 Sep;47(12):3129–34.

34. Yang H, Xu X, Bullock W, Main RP. Adaptive changes in micromechanical environments of cancellous and cortical bone in response to in vivo loading and disuse. J Biomech. 2019 May 24;89:85–94.

35. Kusins J, Knowles N, Targosinski J, Columbus M, Athwal GS, Ferreira L. 3D strain analysis of trabecular bone within the osteoarthritic humeral head subjected to stepwise compressive loads. J Mech Behav Biomed Mater. 2022 Jan;125:104922.

36. Xiong Z, Rouquier L, Chappard C, Bachy M, Huang X, Potier E, et al. A New Microarchitecture-Based Parameter to Predict the Micromechanical Properties of Bone Allografts. Materials. 2023 Jan;16(9):3349.

37. Mitton D, Rappeneau J, Bardonnet R. Effect of a supercritical CO2 based treatment on mechanical properties of human cancellous bone. Eur J Orthop Surg Traumatol. 2005 Dec 1;15(4):264–9.

38. Vastel L, Masse C, Crozier E, Padilla F, Laugier P, Mitton D, et al. Effects of gamma irradiation on mechanical properties of defatted trabecular bone allografts assessed by speed-of-sound measurement. Cell Tissue Bank. 2007 Sep 1;8(3):205–10.

39. Maas SA, Ellis BJ, Ateshian GA, Weiss JA. FEBio: Finite Elements for Biomechanics. J Biomech Eng [Internet]. 2012 Feb 9 [cited 2023 Feb 15];134(1). Available from: https://doi.org/10.1115/1.4005694

40. Iolascon G, Resmini G, Tarantino U. Mechanobiology of bone. Aging Clin Exp Res. 2013 Oct 1;25(1):3–7.

41. Whitaker S. Flow in porous media I: A theoretical derivation of Darcy's law. Transp Porous Media. 1986 Mar 1;1(1):3–25.

42. Chappard C, Marchadier A, Benhamou L. Interindividual and intraspecimen variability of 3-D bone microarchitectural parameters in iliac crest biopsies imaged by conventional micro-computed tomography. J Bone Miner Metab. 2008 Sep 1;26(5):506–13.

43. Olivares AL, Marsal È, Planell JA, Lacroix D. Finite element study of scaffold architecture design and culture conditions for tissue engineering. Biomaterials. 2009 Oct;30(30):6142–9.

44. Kong D, Wang Q, Huang J, Zhang Z, Wang X, Han Q, et al. Design and manufacturing of biomimetic scaffolds for bone repair inspired by bone trabeculae. Comput Biol Med. 2023 Oct 1;165:107369.

45. Mohol SS, Kumar M, Sharma V. PLA-based nature-inspired architecture for bone scaffolds: A finite element analysis. Comput Biol Med. 2023 Sep;163:107163.

46. d'Adamo A, Salerno E, Corda G, Ongaro C, Zardin B, Ruffini A, et al. Experimental measurements and CFD modelling of hydroxyapatite scaffolds in perfusion bioreactors for bone regeneration. Regen Biomater. 2023 Jan 17;10:rbad002.

47. Pires T, Dunlop JWC, Fernandes PR, Castro APG. Challenges in computational fluid dynamics applications for bone tissue engineering. Proc R Soc Math Phys Eng Sci. 2022;478(2257):20210607.

48. Foroughi AH, Liu D, Razavi MJ. Simultaneous optimization of stiffness, permeability, and surface area in metallic bone scaffolds. Int J Eng Sci. 2023 Dec;193:103961.

49. Ali D, Ozalp M, Blanquer SBG, Onel S. Permeability and fluid flow-induced wall shear stress in bone scaffolds with TPMS and lattice architectures: A CFD analysis. Eur J Mech - BFluids. 2020 Jan 1;79:376–85.

50. Karaman D, Ghahramanzadeh Asl H. The effects of sheet and network solid structures of similar TPMS scaffold architectures on permeability, wall shear stress, and velocity: A CFD analysis. Med Eng Phys. 2023 Aug;118:104024.

51. Akerkouch L, Jasuja H, Katti K, Katti D, Le T. The Influence of Fluid Shear Stress on Bone and Cancer Cells Proliferation and Distribution. Ann Biomed Eng. 2023 Jun 1;51(6):1199–215.

52. Pieuchot L, Marteau J, Guignandon A, Dos Santos T, Brigaud I, Chauvy PF, et al. Curvotaxis directs cell migration through cell-scale curvature landscapes. Nat Commun. 2018 Sep 28;9(1):3995.

53. Bidan CM, Kommareddy KP, Rumpler M, Kollmannsberger P, Fratzl P, Dunlop JWC. Geometry as a Factor for Tissue Growth: Towards Shape Optimization of Tissue Engineering Scaffolds. Adv Healthc Mater. 2013;2(1):186–94.

54. Yang Y, Xu T, Bei HP, Zhang L, Tang CY, Zhang M, et al. Gaussian curvature–driven direction of cell fate toward osteogenesis with triply periodic minimal surface scaffolds. Proc Natl Acad Sci. 2022 Oct 11;119(41):e2206684119.

55. Li Z, Chen Z, Chen X, Zhao R. Effect of Surface Curvature on the Mechanical and Mass-Transport Properties of Additively Manufactured Tissue Scaffolds with Minimal Surfaces. ACS Biomater Sci Eng. 2022 Apr 11;8(4):1623–43.

56. Callens SJP, Uyttendaele RJC, Fratila-Apachitei LE, Zadpoor AA. Substrate curvature as a cue to guide spatiotemporal cell and tissue organization. Biomaterials. 2020 Feb;232:119739.

57. Callens SJP, Fan D, van Hengel IAJ, Minneboo M, Díaz-Payno PJ, Stevens MM, et al. Emergent collective organization of bone cells in complex curvature fields. Nat Commun. 2023 Mar 3;14(1):855.

58. Ller RM, Campenhout HV, Damme BV, Hildebrand T, Egsegger PR. Morphometric Analysis of Human Bone Biopsies: A Quantitative Structural Comparison of Histological Sections and Micro-Computed Tomography. 1998;23(1):8.

59. Hildebrand T, Laib A, Müller R, Dequeker J, Rüegsegger P. Direct Three-Dimensional Morphometric Analysis of Human Cancellous Bone: Microstructural Data from Spine, Femur, Iliac Crest, and Calcaneus. J Bone Miner Res. 1999;14(7):1167–74.

Corresponding author:
Professor Thierry Hoc,
Laboratory of Bioengineering and Biomechanics for Bone and Articulations; UMR 7052, CNRS, Paris Diderot University, Sorbonne Paris-Cité, 10 avenue de Verdun 75010 Paris, France
E-mail: Thierry.hoc@cnrs.fr

To cite this article: Zhuang Xiong, Léa Rouquier, Xingrong Huang, Esther Potier, Morad Bensidhoum, Thierry Hoc, Porosity and surface curvature effects on the permeability and wall shear stress of trabecular bone: guidelines for biomimetic scaffolds for bone repair, Computers in Biology and Medicine (177), May 2024,
DOI https://doi.org/10.1016/j.compbiomed.2024.108630

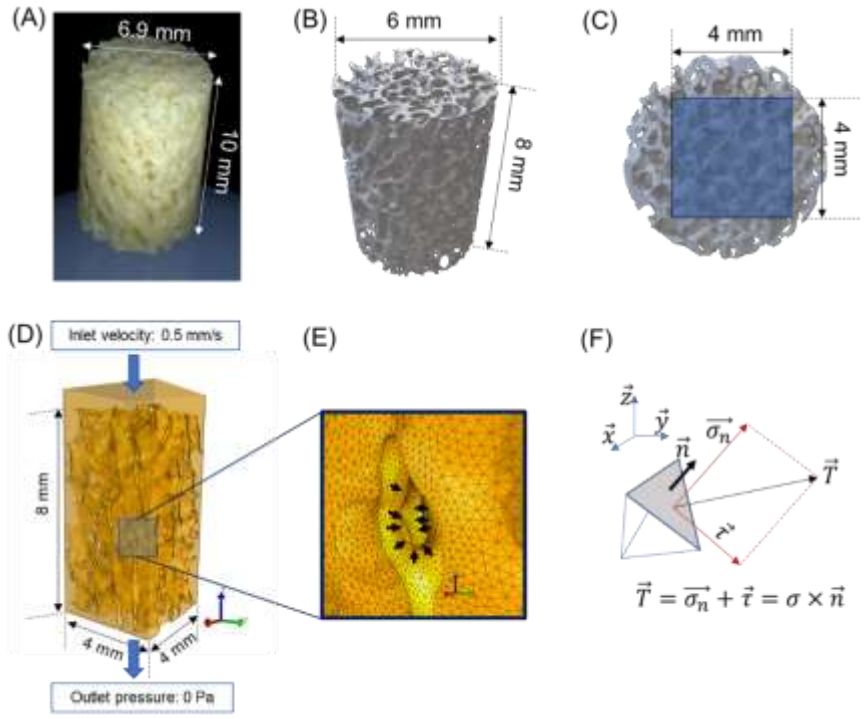

Figure 1: Method overview: representative image of (A) gross image of bone allograft; (B) reconstructed cylindrical volume from µCT imaging; (C) region of interest selected for CFD simulation; (D) CFD simulation model with boundary conditions; (E) meshed model with different individual surface normal (arrows); (F) wall shear stress calculation for individual finite element.

Sample size	BV/TV (%)	Number of mesh elements	Number of skin surface elements	Permeability (10^{-9} m^2)	Average WSS (mPa)
29	28.95 ± 6.10	9240469 ± 629737	1380499 ± 245923	3.69 ± 2.64	6.43 ± 2.16

Table 1: BV/TV, meshing information, permeability, and WSS for the twenty-nine samples, in the form of average value ± standard deviation

Notation	Concave	Hyper	Convex
Surface curvature range	k1>0, k2>0	k1>0, k2<0	k1<0, k2<0
Surface features for fluid domain	Concave ellipsoid	Hyperboloid surface	Convex ellipsoid
Geometry illustration	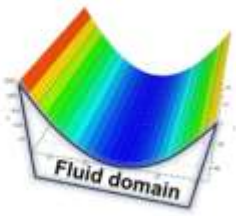	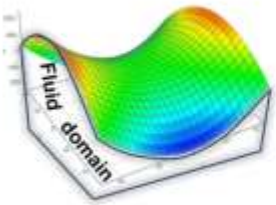	

Table 2: Three different surface curvature features observed in allografts

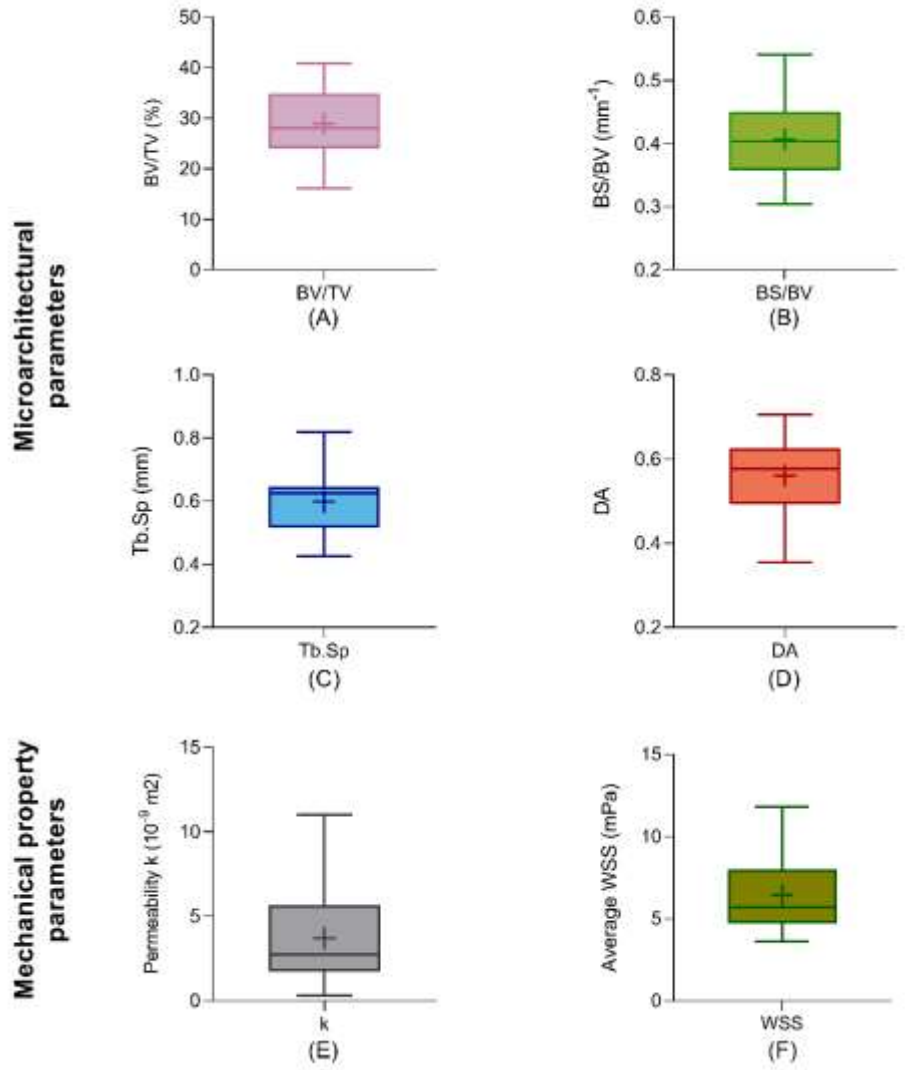

Figure 2: Microarchitectural parameters obtained from micro-CT images and mechanical property parameters derived from CFD analysis; box center lines, bound of boxes and whiskers indicate median, first and third quartiles and minima and maxima within a 1.5 times interquartile range (IQR), respectively. +: mean value, N=29. (A) bone volume fraction (%, BV/TV); (B) bone surface area to volume ratio (mm-1, BS/BV); (C) trabecular separation (mm, Tb.Sp); (D) degree of anisotropy (DA); (E) average wall shear stress (mPa, WSS); (F) permeability (10-9 m2, k).

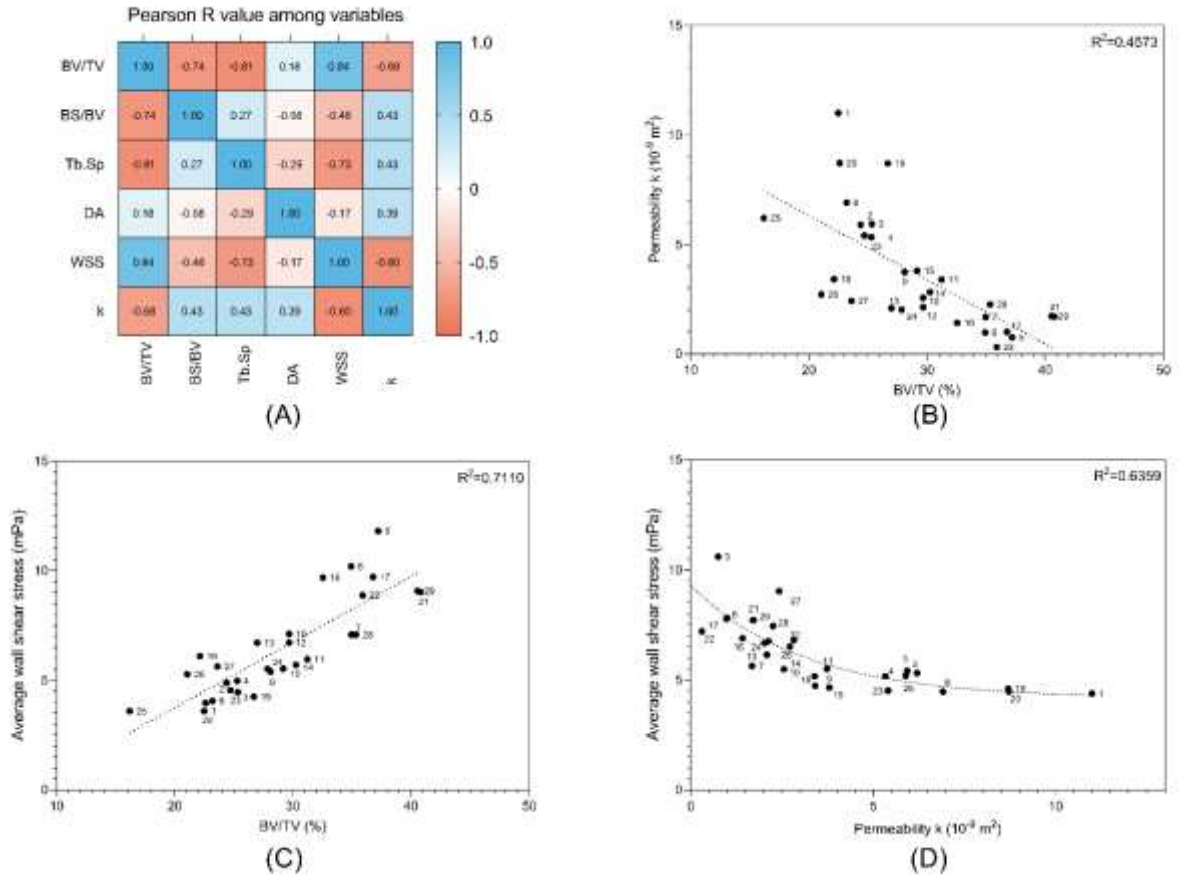

Figure 3: Correlation relation among variables. (A) Correlation matrix heatmap of Pearson's R value for parameters employed in the present study; (B) Pearson's linear regression between BV/TV and k; (C) Pearson's linear regression between BV/TV and average WSS; (D) Non-linear exponential regression between k and average WSS.

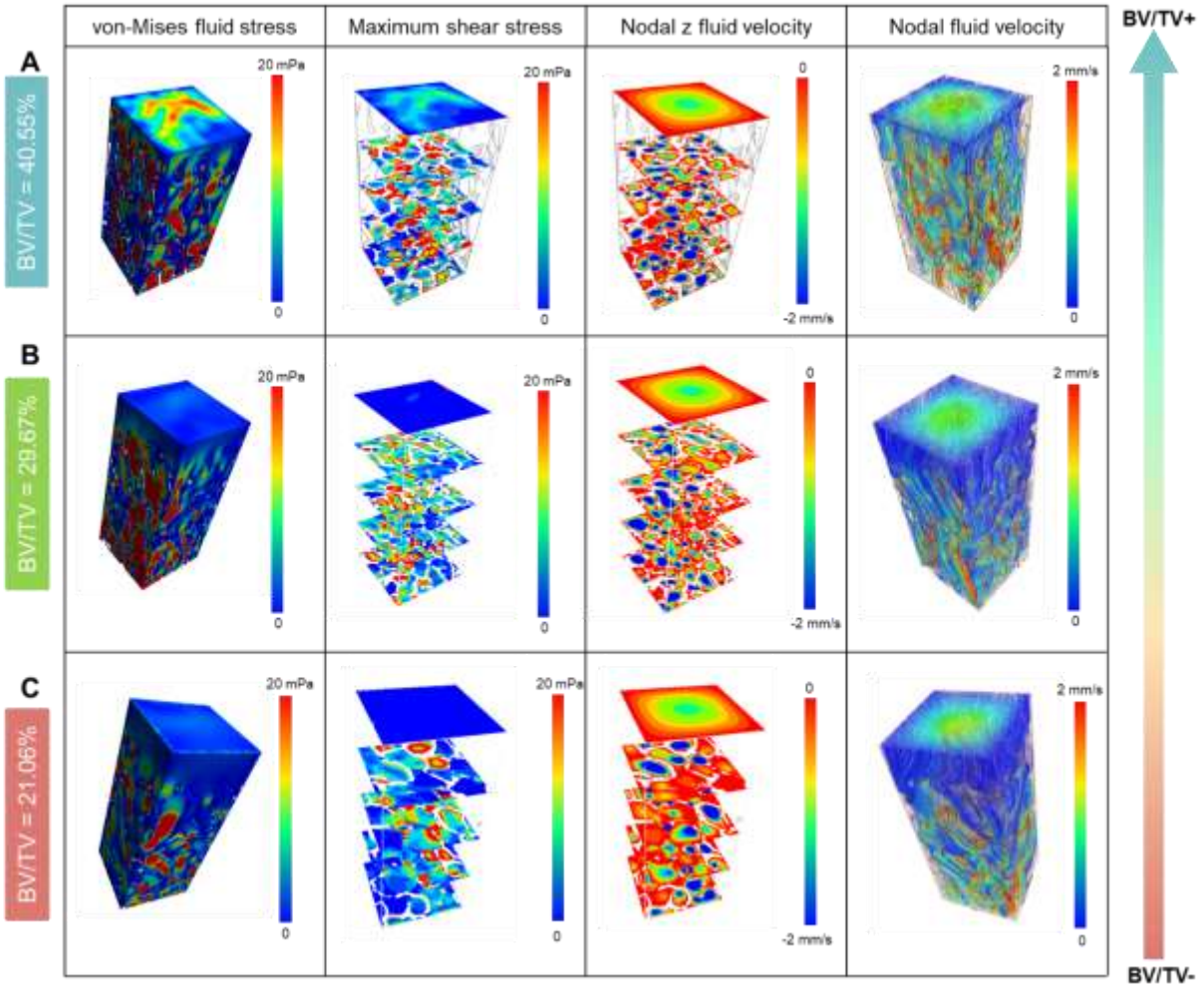

Figure 4: CFD simulation results of von-Mises fluid stress distribution color map, max shear stress distribution slice plot, nodal z fluid velocity distribution slice plot, and fluid velocity streamline plot for three representative samples with varying BV/TV. (A) sample n°29 with BV/TV = 40.55%, the simulation element size is of 4 mm * 4 mm * 8.5 mm (homogeneous flow layer included); (B) sample n°10 with BV/TV = 29.67%, the simulation element size is of 4 mm * 4 mm * 9 mm (homogeneous flow layer included); (C) sample n°26 with BV/TV = 21.06%, the simulation element size is of 4 mm * 4 mm * 9.5 mm (homogeneous flow layer included). The distance between the five image sections is equally distributed along the model height.

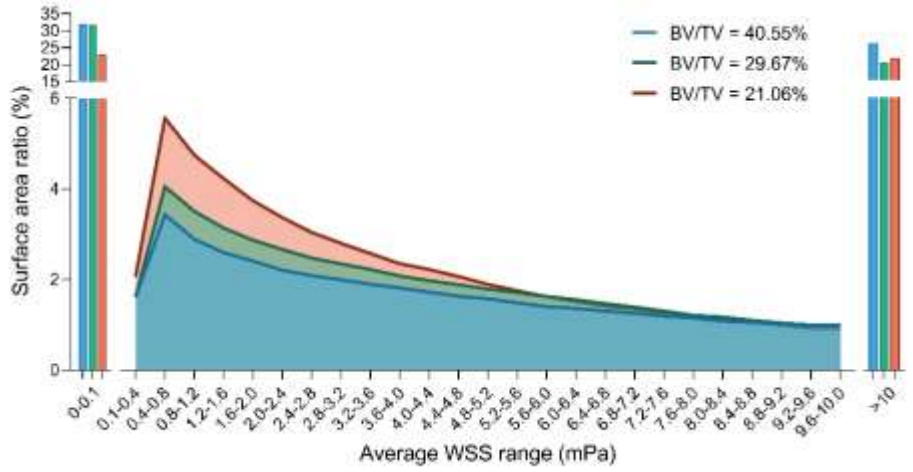

Figure 5: WSS distribution plot for three representative samples with varying BV/TV (sample n°29 with BV/TV = 40.55%; sample n°10 with BV/TV = 29.67%; sample n°26 with BV/TV = 21.06%).

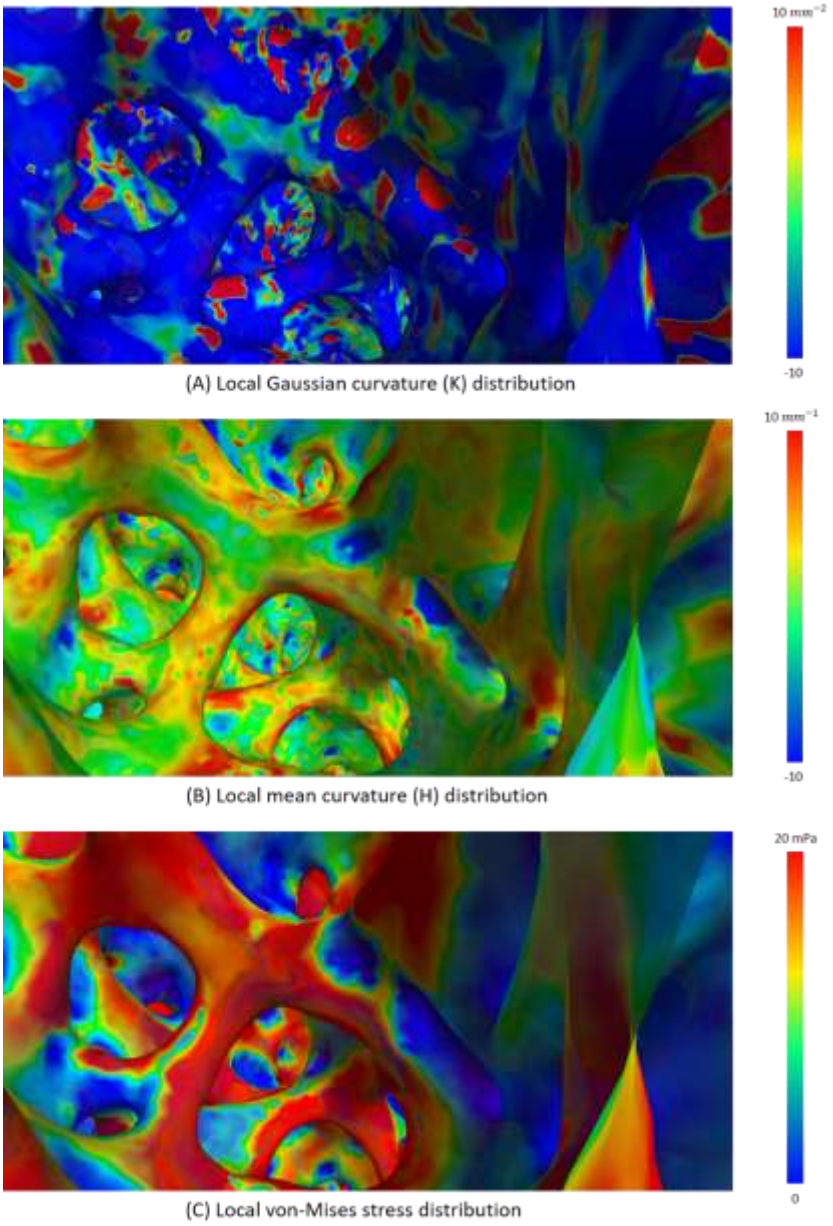

Figure 6: Distribution of local surface curvatures and fluid-induced stress for a randomly chosen local fluid domain. (A) local distribution of the Gaussian curvature K of the fluid domain; (B) local distribution of the mean curvature H of the fluid domain; (C) local distribution of the von-Mises stress of the fluid domain.

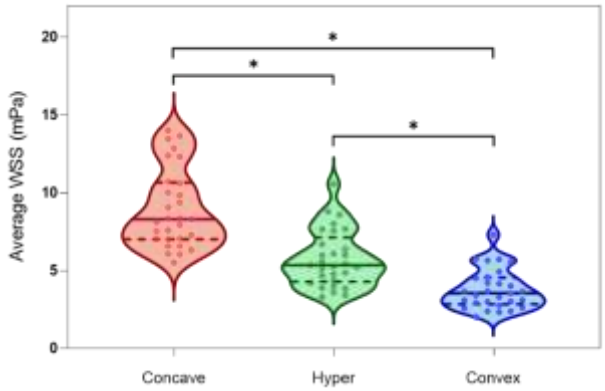

Figure 7: The average WSS in the three selected surface curvature regions of the fluid domain (Concave, Hyper, Convex) for the 29 samples. Solid line and dotted line represent the median value and the quartiles, respectively. *: $p < 0.05$ by Mann-Whitney test.

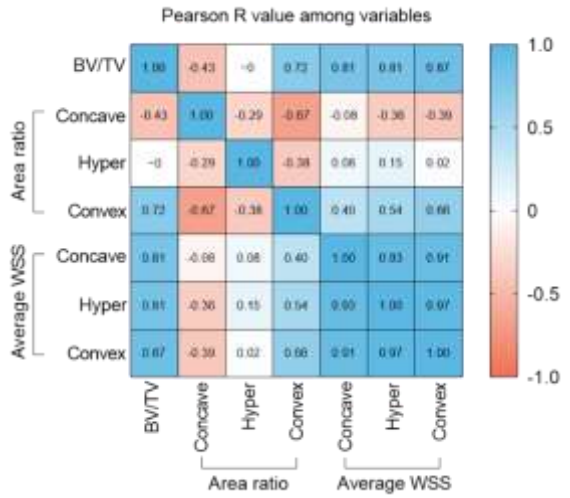

Figure 8: Correlation matrix heatmap for BV/TV, the area ratio, and the average wall shear stress for each of the three selected surface curvature regions of the fluid domain (Concave; Hyper; Convex:).

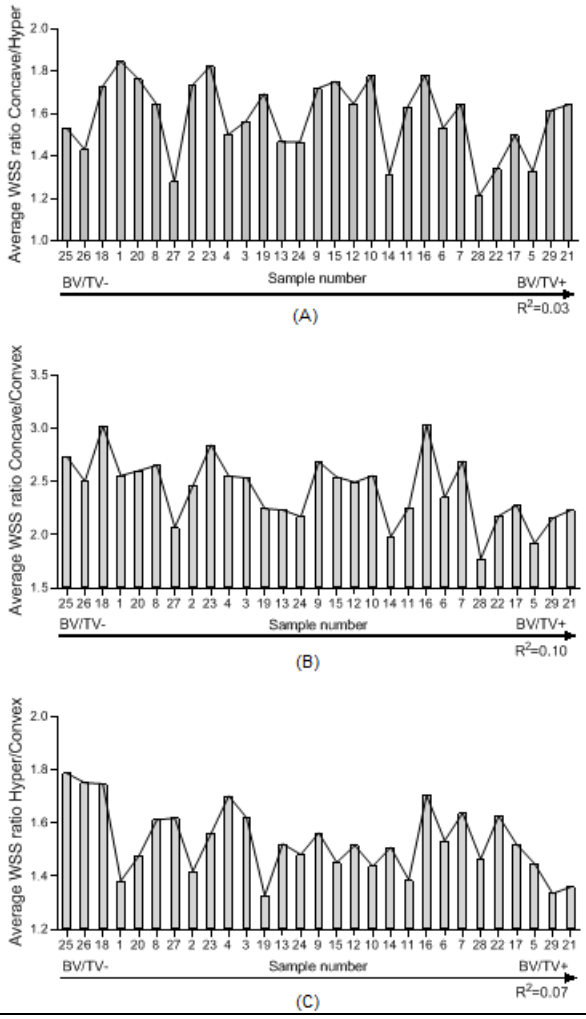

Supplementary Data: Figure 9: Histograms of the average wall shear stress ratio for the three different curvature regions and its correlation with BV/TV of individual sample: the samples are aligned in regards to their BV/TV value from the smallest at left to the greatest at right, R-squared values are obtained from Pearson's linear regression. (A) Average wall shear stress ratio of concave (k1>0, k2>0) region and Hyper (k1>0, k2<0) region; (B) Average wall shear stress ratio of concave (k1>0, k2>0) region and convex (k1<0, k2<0) region; (C) Average wall shear stress ratio of Hyper (k1>0, k2<0) region and convex (k1<0, k2<0) region.

Sample n°	BV/TV (%)	Mesh elements	Wall elements	Permeability (10e-9 m2)	Average WSS (mPa)
1	22.49	8974024	1100905	10.99	3.59
2	24.39	9566049	1294282	5.89	4.88
3	25.34	9237719	1183502	5.93	4.45
4	25.29	9303155	1237125	5.34	4.97
5	37.21	9056508	1525989	0.75	11.81
6	34.92	9431330	1609741	0.97	10.20
7	34.96	9259306	1573508	1.68	7.08
8	23.19	8563035	1062851	6.91	4.06
9	28.11	9090090	1286351	3.74	5.40
10	29.67	10352564	1808776	2.56	7.12
11	31.23	9414032	1504973	3.39	5.96
12	29.67	9723722	1518655	2.13	6.72
13	26.98	9750759	1538658	2.08	6.71
14	30.26	8743058	1261710	2.82	5.70
15	29.17	9938190	1590723	3.80	5.53
16	32.55	10840037	1868472	1.42	9.68
17	36.77	9422234	1626856	1.00	9.71
18	22.13	10623055	1600780	3.41	6.10
19	26.69	8956657	1146498	8.70	4.25
20	22.61	9025776	1166500	8.72	3.96
21	40.79	9025641	1608505	1.70	9.02
22	35.89	9115621	1571079	0.30	8.87
23	24.71	9104177	1221280	5.41	4.55
24	27.86	8345819	1105712	2.02	5.52
25	16.18	8338086	914832	6.20	3.59
26	21.06	9194110	1219812	2.72	5.27
27	23.61	8166704	992972	2.42	5.63
28	35.34	8373492	1290798	2.26	7.07
29	40.55	9038645	1602142	1.72	9.08

Supplementary Data: Table 3

Sample n°	Area average WSS (mPa)			Area to wall surface ratio		
	Concave	Hyper	Convex	Concave	Hyper	Convex
1	6.07	3.28	2.37	0.12	0.73	0.11
2	7.57	4.37	3.08	0.11	0.74	0.11
3	6.56	4.19	2.59	0.09	0.78	0.09
4	6.99	4.66	2.74	0.08	0.80	0.08
5	13.99	10.55	7.29	0.07	0.75	0.15
6	13.46	8.79	5.73	0.09	0.74	0.14
7	9.83	5.98	3.65	0.08	0.77	0.12
8	6.31	3.83	2.38	0.10	0.74	0.11
9	8.34	4.85	3.11	0.10	0.73	0.12
10	10.60	5.96	4.15	0.11	0.75	0.11
11	8.29	5.09	3.67	0.11	0.73	0.13
12	9.99	6.07	4.01	0.10	0.74	0.13
13	9.35	6.38	4.19	0.10	0.76	0.11
14	7.01	5.33	3.53	0.07	0.76	0.14
15	8.34	4.76	3.28	0.12	0.75	0.11
16	13.64	7.67	4.50	0.15	0.77	0.08
17	12.84	8.57	5.64	0.10	0.74	0.13
18	9.03	5.22	2.99	0.16	0.74	0.07
19	6.57	3.88	2.92	0.11	0.73	0.12
20	6.03	3.42	2.32	0.13	0.73	0.10
21	12.38	7.54	5.55	0.09	0.74	0.15
22	10.70	7.99	4.91	0.08	0.75	0.13
23	7.27	3.99	2.56	0.13	0.72	0.11
24	7.92	5.41	3.65	0.09	0.72	0.15
25	5.49	3.59	2.01	0.12	0.75	0.08
26	7.51	5.25	3.00	0.10	0.76	0.10
27	7.06	5.52	3.41	0.08	0.76	0.12
28	8.10	6.69	4.57	0.06	0.74	0.16
29	12.30	7.62	5.71	0.09	0.74	0.15

Supplementary Data: Table 4